Title: Synchrotron radiation-based X-ray tomography reveals life history in primate cementum incrementation

Elis Newham[1,2*], Ian J. Corfe[3,4], Kate Robson Brown[1,5], Neil J. Gostling[6], Pamela G. Gill[7,8], Philipp Schneider[2*].

1. Department of Anthropology and Archaeology, University of Bristol, Bristol, UK.
2. Bioengineering Science Research Group, Faculty of Engineering and Physical Sciences, University of Southampton, Southampton, UK.
3. Institute of Biotechnology, University of Helsinki, Helsinki, Finland.
4. Geological Survey of Finland, Espoo, Finland.
5. Department of Mechanical Engineering, University of Bristol, Bristol, UK.
6. Faculty of Environmental and Life Sciences, University of Southampton, Southampton, UK.
7. School of Earth Sciences, University of Bristol, Bristol, UK.
8. Earth Science Department, The Natural History Museum, London, UK.

Abstract (200 words max)

Cementum is a mineralised dental tissue common to mammals that grows throughout life, following a seasonally appositional rhythm. Each year, one thick translucent increment and one thin opaque increment is deposited, offering a near-complete record of an animal's life history. Male and female mammals exhibit significant differences in oral health, due to the contrasting effects of female versus male sex hormones. Oestrogen and progesterone have a range of negative effects on oral health, that extends to the periodontium and cementum growth interface. Here, we use synchrotron radiation-based X-ray tomography to image the

cementum of a sample of rhesus macaque (*Macaca mulatta*) teeth from individuals of known life history. We found that increased breeding history in females corresponds with increased increment tortuosity and less organised cementum structure, when compared to male and juvenile cementum. We quantified structural differences by measuring the greyscale 'texture' of cementum and comparing results using principal components analysis. Adult females and males occupy discrete regions of texture space with no overlap. Females with known pregnancy records also have significantly different cementum when compared with non-breeding and juvenile females. We conclude that several aspects of cementum structure and texture may reflect differences in sexual life history in primates.

Keywords

Cementum, mammal, sex hormones, life history, synchrotron radiation computed tomography,

1. Introduction

Cementum, the connective tissue that anchors tooth roots to the periodontal ligament (PDL), is unique amongst mammalian dental tissues, as its growth is continuous throughout life, recorded by a series of circum-annual growth increments (1). Every year of life is recorded by one wide translucent increment and one narrow opaque increment, when viewed under transmitted light in thin-section histology (2). Unfavourable seasons are thought to promote a reduction in the deposition rate of the cementum hydroxyapatite matrix, while the mineralisation rate is unaffected, producing ultra-mineralisation of narrow cementum increments during these seasons (3,4), though there is still uncertainty as to whether narrow or wide increments are more mineralised (2,5).

As the only mineralised dental tissue to grow throughout life without remodelling (apart from instances of severe gingival damage; Fig. 1a) (4,6), cementum is likely to be affected by several aspects of life history. As cementum receives collagenous 'Sharpey's fibres' from the PDL, its growth is also affected by periodontal health and disease (6). It is widely accepted in clinical literature that females encounter higher rates of periodontal and dental disease than males, and studies on laboratory animal populations show that instances of dental disease increase proportionally with increasing levels of the female sex hormones oestrogen and progesterone (Fig. 1a) (7-9). Conversely, increases in androgen levels (male sex hormones) have no significant effect on oral health (9). The negative impacts of oestrogen on oral health have also been shown to fluctuate through the menstrual cycle (9) and accelerate during puberty and pregnancy. Damage to the gingiva related to oestrogen and progesterone extends to the PDL and its connective tissues, supressing collagen production and breaking down collagen fibres (7) (Fig. 1a).

A major constraint of cementum studies is the restrictive nature of thin-section imaging, which provides a limited number of two-dimensional (2D) viewpoints of the tissue, but synchrotron radiation-based computed tomography (SRCT) applications have overcome this caveat (4,10). A preliminary report (11) attempted to use SRCT to compare cementum between male and female archaeological humans, and, although a single increment of potentially abnormal shape/structure was identified in the cementum of one female, taphonomic alteration and low image quality meant the data was insufficient to confidently identify it as a stress marker linked to a pregnancy event. Several earlier, non-SRCT studies, have identified dimorphic characteristics of cementum between sexually mature male and female cementum in a range of mammals (12-14). These studies, however, are unable to provide predictive means of identifying sex in individuals of unknown life history.

To address these challenges, we present the results of a preliminary experiment employing propagation-based phase contrast imaging (PPCI) through SRCT (herein PPCI-CT) to characterise the cementum of 14 rhesus macaque (*Macaca mulatta*) individuals of known life history and sex. We subject PPCI-CT data to a novel image processing and analysis protocol to measure the shape of increments, and the texture of cementum for the first time, to compare these properties between individuals and test for significant differences between sexes.

2. Methods

Macaca mulatta sample

Lower right first molar teeth (m1) were extracted from a sample of deceased macaques with monitored life history (see Supplement for further detail). The sample comprised nine sexually active females, three sexually inactive females, one sexually mature male and one juvenile female (Table 1). The crown of each tooth was removed, and anterior/posterior roots were mechanically separated and glued to carbon fibre rods (2 mm diameter) for PPCI-CT imaging.

Image acquisition, processing and analysis

PPCI-CT data was collected from the TOMCAT beamline of the Swiss Light Source (Paul Scherrer Institute; Villigen, Switzerland) (see Supplement). The axial third of each root was imaged at an isotropic voxel size of 650 nm, with 20 keV X-ray energy of 20 keV, integration time of 150 ms for 1500 angular projections, at 14-mm sample-to-detector distance. X-ray projection phase was retrieved using the Paganin single-distance phase retrieval algorithm, implemented in-house at TOMCAT, using $\beta=3.7\ 10^{-8}$ for the imaginary part, and $\delta=1.7\ 10^{-10}$ for the decrement of the real part of the refractive index (15) (Fig. 1b-c). Phase-retrieved

projections were reconstructed using an in-house implementation of the Gridrec algorithm (16) at TOMCAT.

We present here a novel protocol for standardised analysis and comparison of discrete properties of cementum that directly relate to its growth through life (see Supplement). For each individual, PPCI-CT cementum data was selected from 30 random CT slices. These slices were investigated for the predominance of cellular voids. If >10 voids were found in a slice, they were deemed evidence of cellular cementum and the respective slice was replaced with another randomly selected PPCI-CT slice, so that only circum-annually deposited acellular cementum was compared (1). Cementum in the selected data was straightened and isolated with the 'straighten' function in ImageJ/Fiji (Version 2.0) (17) (see Supplement), using the cemento-dentine junction as a reference for the straightening direction (Fig. 1b-g). Straightened data was then subjected to two custom-designed algorithms in Matlab (R2016a; The MathWorks, Inc., Natick, MA, USA) that assessed cementum texture (Fig. 1d-e) and increment shape (Fig. 1f-i), respectively.

Increment shape was defined as the tortuosity of an increment along its 2D path-length along straightened PPCI-CT slices. Tortuosity is here defined as the ratio between the path length followed by an increment and the shortest possible path length (Fig. 1f-g). The outermost five increments in each randomly selected PPCI-CT slice were isolated (see Supplement), and their path length was calculated as their *x*-axis distance (in pixels), plus the change in *y*-axis values between every concurrent pixel along the *x*-axis (Fig. 1f-i). Shortest path lengths were calculated as the hypotenuse between the *x*/*y*-axis coordinates at the end points of the increment (Fig. 1h-i). Non-parametric Kruskal-Wallis analysis was used to compare tortuosity values between individuals and sub-samples.

Cementum 'texture' was defined as the spatial organisation of greyscale values within the PPCI-CT cementum data. By measuring greyscale as a 'third dimension/z-axis', several metrics commonly used in biological surface profiling were applied to our data (Fig. 1d-e, Table 2) (18). These comprised height measures, spatial measures, hybrid measures and functional measures (see Supplement and references therein for definition different measure types). 20 measures were derived from each PPCI-CT slice which had previously been used to estimate increment tortuosity, each measure was compared between two subsamples (male/adult female) using ANOVA (Table 2), and measures with significant differences (p<0.05) between subsamples were subjected to principal components analysis (PCA).

3. Results

Qualitative comparison between the cementum increments of male and female *Macaca mulatta* individuals suggests several discrete differences between their texture and shape. Male cementum increments follow relatively uniform (low-tortuosity) transects through the tissue and are of roughly equal thickness (Fig. 1b). Female increments are considerably more chaotic and follow conflicting, tortuous transects through the cementum, producing complex patterns and increment splitting/coalescence (Fig. 1c). These effects are compounded through the cementum, often resulting in increased tortuosity in the outermost increment. Increments in samples from female individuals also qualitatively show considerably lower image contrast than male increments and are more poorly organised with higher isotropy than male increments.

Following cementum isolation and straightening, quantitative analysis supports the qualitative inferences of higher increment tortuosity within samples from female individuals (Fig. 2a). Every female individual produced significantly higher values of increment tortuosity than the male individual (Table 1). Samples from breeding adult females also had

146 significantly higher tortuosity than from non-breeding adult females ($H = 438.4$; $p < 0.001$),
147 and the latter in-turn produced significantly higher tortuosity than the juvenile female
148 individual ($H = 18.2$; $p < 0.001$) (Fig. 2a). The female with the highest number of recorded
149 pregnancies (female l59) also produced increments with the highest individual tortuosity, and
150 the highest mean tortuosity was found for female l72, with four recorded pregnancies (Fig.
151 2a, Table 1).
152 Cementum texture also showed significant differences between adult male and female
153 subsamples. Of the 20 assessed texture measures, 17 were significantly different when
154 compared using ANOVA (Table 2). When subjected to PCA, principal component 1 (41.2%
155 of variance) reflected predominantly the image contrast between light/dark increments, with
156 positive values reflecting higher image contrast. Principal component 2 (16.9% of variance)
157 reflected principally the 'surface roughness' of cementum, with lower values corresponding
158 to lower variability in greyscale values and less greyscale anisotropy (directional
159 dependence) throughout the sampled PPCI-CT slice. Male cementum formed its own discrete
160 'texture space', with no overlap between values from male and adult female individuals (Fig.
161 2b). However, male texture space did overlap with juvenile female texture space, which in-
162 turn overlapped with that of non-breeding females, but not breeding females. The texture
163 space of non-breeding females was positioned between that of juvenile female and breeding
164 female cementum. The cementum of l72, the individual with the highest mean increment
165 tortuosity, also produced the most highly differentiating texture measure when compared to
166 the male individual (Fig. 2b).
167
168 **4. Discussion**
169 We here demonstrate a significant relationship between sexual life history and patterns in
170 cementum incrementation in a dataset of *Macaca mulatta* individuals. We interpret these

differences in tortuosity and texture as reflecting sexual differences in the growth and maintenance of cementum due to distinct hormonal regimes, with an increasing influence of oestrogen and progesterone creating different conditions for cementum growth in females. Pregnancy is known to promote a significant increase in oestrogen and progesterone, as is the onset of sexual maturity. Hence, our hypothesis is further supported by the findings of significant differences between the tortuosity of increments found in breeding *versus* non-breeding females, and adult females *versus* the juvenile female. This pattern correlates with the occupation of texture space, with breeding females occupying the furthest texture space from male cementum, bridged by cementum signals from non-breeding and then juvenile cementum.

Our novel methods for image processing, analysis and validation have the potential to elucidate quantitative differences in cementum organisation between/within populations, and offer a new way to relate cementum growth to a range of life history variables and events. If the sexual dimorphism we identify here is retained in larger samples of known life history, these methods, in combination with increment counting using non-destructive SRCT imaging, have the potential for estimating life history data for individuals and populations of unknown provenance, including archaeological, palaeontological and forensic samples.

188 **Figure legends**

189 **Figure 1. Exploring the relationship between hormonal physiology and cementum**
190 **increment tortuosity and cementum texture in propagation-based phase contrast**
191 **imaging (PPCI) CT data of *Macaca mulatta* cementum. a**, Flow chart describing potential
192 negative effects of major female sexual hormones on oral health (green boxes) and their
193 causes (orange boxes) (7-9). **b-c**, PPCI-CT slices of male (individual k39) (**b**) and female
194 (individual l56) (**c**) tooth roots. Insets in **b-c** are straightened and isolated reconstructions of
195 cementum following the cemento-dentine boundary (red bracketed lines), with individual
196 increments highlighted (red arrows). **d-e**, Heatmaps of greyscale values for straightened male
197 (**e)** and female (**f**) cementum. **f-g**, Outlines of outermost increment in straightened cementum
198 following dashed red lines for male (**f**) and female (**g**). **h-i,** Relationship between increment
199 length (red line) and shortest possible length (dashed white line) in male (**h**) and female
200 cementum (**i**).

201 **Figure 2. Cementum increment tortuosity and texture results. a**, Boxplots of tortuosity
202 measurements for each *Macaca mulatta* individual. Red boxes: breeding adult females;
203 orange boxes: non-breeding adult female; purple box: juvenile female; blue box: adult male.
204 Thick black lines represent mean values, upper and lower box bounds represent upper and
205 lower quartile ranges. **b**, Results of principal components analysis of 17 texture measures for
206 cementum of each *M. mulatta* individual. **c,** Correlation plot of texture metrics along PC1. **d**,
207 Correlation plot of texture metrics along PC2.

208

209 **Table legends.**

210 **Table 1.** Life history data and tortuosity comparisons for *Macaca mulatta* specimens.

211 **Table 2.** Cementum texture measure descriptions and results of ANOVA comparisons and
212 PCA correlations between measurements for the adult female subsample (breeding and non-

breeding) and adult male individual. See Supplement for description and explanation of measures.

Acknowledgements and funding: This study was part-funded by a Natural Environmental Research Council/Engineering and Physical Sciences Research Council doctoral candidateship (UK; grant number NE/R009783/1). Funding was also provided by Ginko Investments Ltd, Bristol, UK. We acknowledge the Paul Scherrer Institute, Villigen, Switzerland for provision of synchrotron radiation beamtime at the TOMCAT beamline of the SLS (Experiment 20151391) and would like to thank Iwan Jerjen, Orestis Katsamenis, Mark Mavrogordato, Sharif Ahmed, Juan Núñez, Christianne Fernee and Priscilla Bayle for their assistance during our beamtime.

Conflict of interest. The authors report no conflicts of interest.

Author contributions. EN secured and prepared all specimens and designed, validated and performed all automated analyses. All authors were involved in writing the proposal for synchrotron beamtime and the synchrotron beamtime. All authors contributed to writing the manuscript.

Data availability. Data supporting this study are openly available from the University of Southampton repository (https://doi.org/10.5258/SOTON/D1467).

References

1. Naji, S., Colard, T., Blondiaux, J., Bertrand, B., d'Incau, E., Bocquet-Appel, J. P. (2016). Cementochronology, to cut or not to cut? *International Journal of Paleopathology.* **15**, 113-119.

2. Dean, C., Le Cabec, A., Spiers, K., Zhang, Y., Garrevoet, J. (2018). Incremental distribution of strontium and zinc in great ape and fossil hominin cementum using synchrotron X-ray fluorescence mapping. *Journal of the Royal Society Interface.* **15**(138), 20170626.
3. Lieberman, D. E. (1993). Life history variables preserved in dental cementum microstructure. *Science.* **261**(5125), 1162-1164.
4. Le Cabec, A., Tang, N. K., Ruano Rubio, V., Hillson, S. (2019). Nondestructive adult age at death estimation: visualizing cementum annulations in a known age historical human assemblage using synchrotron X-ray microtomography. *American Journal of Physical Anthropology.* **168**(1), 25-44.
5. Stock, S. R., Finney, L. A., Telser, A., Maxey, E., Vogt, S., Okasinski, J. S. (2017). Cementum structure in Beluga whale teeth. *Acta Biomaterialia.* **48**, 289-299.
6. Surarit, R., Krishnamra, N., & Seriwatanachai, D. (2016). Prolactin receptor and osteogenic induction of prolactin in human periodontal ligament fibroblasts. *Cell Biology International*, **40**(4), 419–427.
7. Silk, H., Douglass, A. B., Douglass, J. M., & Silk, L. (2008). Oral health during pregnancy. *American Family Physician*, **77**(8), 1139-1144.
8. Liu, F. T. Y., & Lin, H. S. (1973). Effect of the Contraceptive Steroids Norethynodrel and Mestranol on Dental Caries Activity in Young Adult Female Rats. *Journal of Dental Research*, **52**(4), 753–757.
9. Lukacs, J. R., & Largaespada, L. L. (2006). Explaining Sex Differences in Dental Caries Prevalence: Saliva, Hormones, and "Life-History" Etiologies. *American Journal of Human Biology*, **18**, 540-555.
10. Newham, E., Gill, P.G., Brewer, P., Benton, M.J., Fernandez, V., Gostling, N.J., Haberthür, D., Jernvall, J., Kankanpää, T., Kallonen, A., *et al*. (2019). Reptile-like

physiology in Early Jurassic stem-mammals. *bioRxiv*, DOI:10.1101/785360 (in review for *Nature Communications*).

11. Mani-Caplazi, G., Schulz, G., Deyhle, H., Hotz, G., Vach, W., Wittwer-Backofen, U. and Müller, B., 2017. Imaging of the human tooth cementum ultrastructure of archeological teeth, using hard x-ray microtomography to determine age-at-death and stress periods. In *Developments in X-Ray Tomography XI* (Vol. 10391, p. 103911C). International Society for Optics and Photonics.
12. Kolb, H. (1978). The formation of lines in the cementum of premolar teeth in foxes. *Journal of Zoology*, **185**(2), 259–263
13. Kvam, T. (1984). Age determination in European lynx *Lynx lynx* by incremental lines in tooth cementum. *Acta Zoologica Fennica*, **171**, 221–223.
14. Medill, S., Derocher, A. E., Stirling, I., & Lunn, N. (2010). Reconstructing the reproductive history of female polar bears using cementum patterns of premolar teeth. *Polar Biology*, **33**(1), 115–124.
15. Paganin, D., Mayo, S. C., Gureyev, T. E., Miller, P. R. & Wilkins, S. W. Simultaneous phase and amplitude extraction from a single defocused image of a homogeneous object. *Journal of Microscopy*, **206**, 33-40 (2002).
16. Marone, F. & Stampanoni, M. Regridding reconstruction algorithm for real-time tomographic imaging. *Journal of Synchrotron Radiation.* **19**, 1029-1037 (2012).
17. Schneider, C. A., Rasband, W. S., & Eliceiri, K. W. (2012). NIH Image to ImageJ: 25 years of image analysis. *Nature Methods*, **9**(7), 671.
18. Purnell, M., Seehausen, O., & Galis, F. (2012). Quantitative three-dimensional microtextural analyses of tooth wear as a tool for dietary discrimination in fishes. *Journal of the Royal Society Interface*, **9**(74), 2225–2233.

Figure 1.

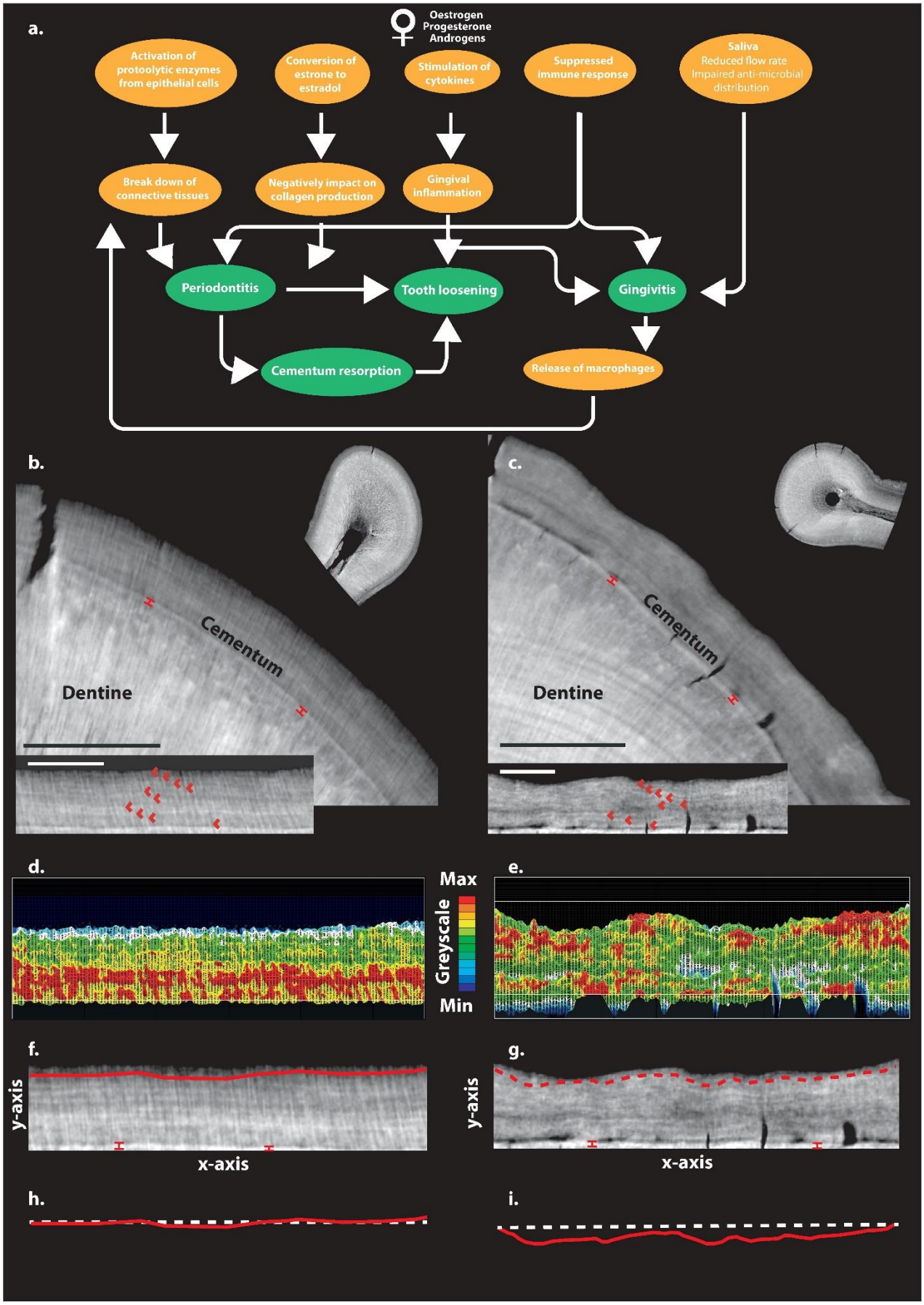
a.
Oestrogen
Progesterone
Androgens
Activation of protoolytic enzymes from epithelial cells
Conversion of estrone to estradol
Stimulation of cytokines
Suppressed immune response
Saliva
Reduced flow rate
Impaired anti-microbial distribution
Break down of connective tissues
Negatively impact on collagen production
Gingival inflammation
Periodontitis
Tooth loosening
Gingivitis
Cementum resorption
Release of macrophages
b.
Cementum
Dentine
c.
Cementum
Dentine
d.
Max
Greyscale
Min
e.
f.
y-axis
x-axis
g.
y-axis
x-axis
h.
i.

287 **Figure 2.**

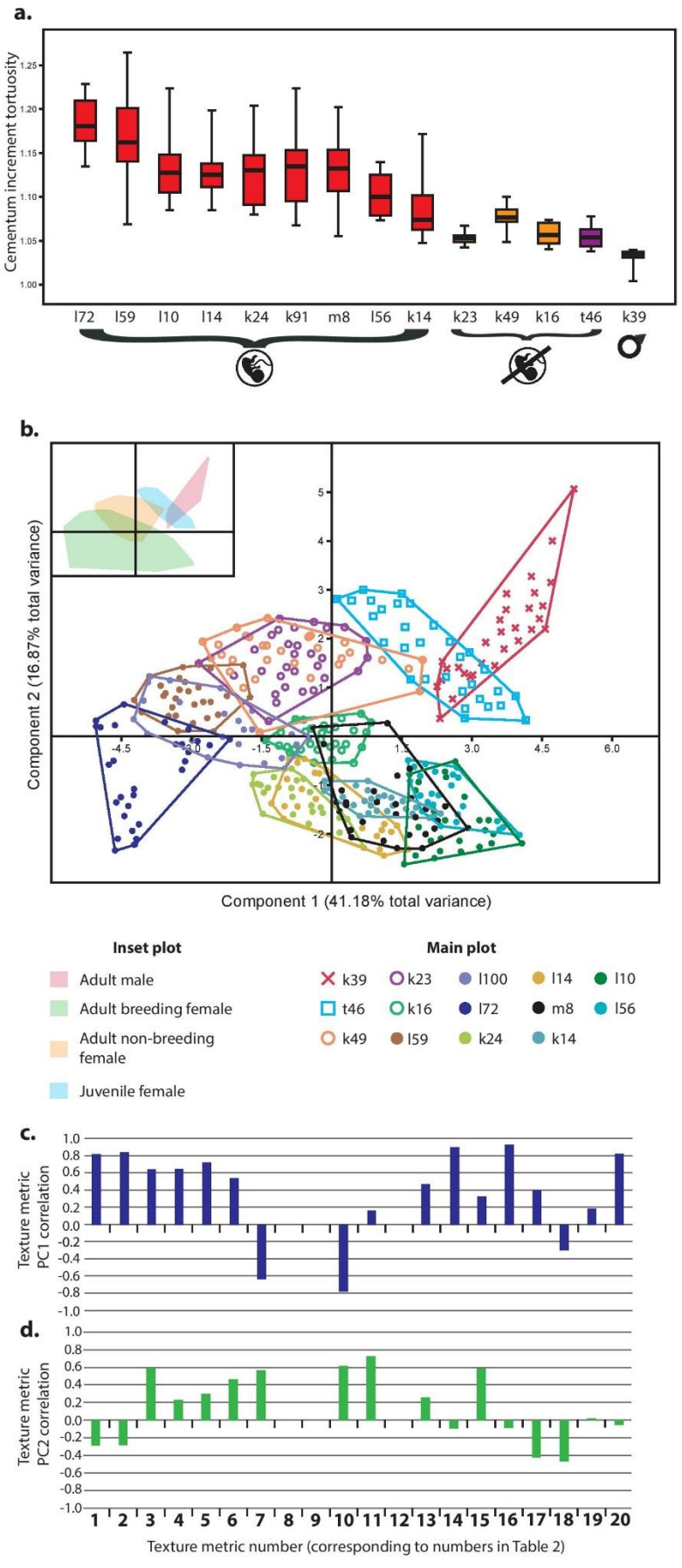

288

289 **Table 1.**

Life history data						Cementum increment tortuosity Kruskal-Wallis comparisons									
Individual	Subsample	Age at death	DOB	DOD	Birth events	vs male		vs female		vs breeding females		vs non-breeding females		vs juvenile	
						H	*p*	*H*	*p*	*H*	*p*	*H*	*p*	*H*	*p*
l72	Breeding adult female	11	29.04.04	08.04.15	29.05.07, 15.03.08, 26.03.10, 27.05.11	82.3	<0.001	82.8	<0.001	75.2	<0.001	118.8	<0.001	84.1	<0.001
l59	Breeding adult female	11	17.04.04	09.04.15	24.06.07, 17.01.09, 07.04.10, 28.03.11, 08.04.12, 24.04.14	143.8	<0.001	205.7	<0.001	163.4	<0.001	296.2	<0.001	148.8	<0.001
l10	Breeding adult female	11	20.02.04	08.04.15	23.06.08, 06.03.10, 14.04.11	142.9	<0.001	2.9	0.089	2.7	0.100	290.4	<0.001	148.2	<0.001
l14	Breeding adult female	12	27.02.04	08.04.15	07.06.07, 05.03.08, 30.06.09, 27.05.10, 05.05.11	137.2	<0.001	1.3	0.261	4.0	0.056	271.0	<0.001	142.0	<0.001
k24	Breeding adult female	12	12.03.03	08.04.15	21.07.08, 22.06.10, 18.05.11	106.8	<0.001	0.2	0.659	2.2	0.139	141.1	<0.001	109.8	<0.001
k91	Breeding adult female	11.5	06.10.03	10.04.15	30.06.08, 03.08.09, 16.06.10, 24.03.11, 02.08.13	135.9	<0.001	3.7	0.054	0.4	0.527	206.6	<0.001	138.9	<0.001
m8	Breeding adult female	9	01.02.08	18.06.15	29.01.09	158.6	<0.001	13.4	<0.001	0.26	0.61	319.4	<0.001	154.0	<0.001
l56	Breeding adult female	11	14.04.04	10.04.15	20.04.08, 12.03.10, 08.07.11	74.9	<0.001	17.8	<0.001	36.3	<0.001	62.7	<0.001	122.0	<0.001
k14	Breeding adult female	11	16.09.04	09.03.15	27.02.14	122.7	<0.001	80.3	<0.001	118.3	<0.001	13.4	<0.001	74.1	<0.001
k23	non-breeding adult female	12	09.03.03	09.04.15	None.	95.2	<0.001	171.6	<0.001	183.8	<0.001	40.9	<0.001	0.004	0.95
k49	non-breeding adult female	12	09.04.03	08.04.15	None.	93.7	<0.001	85.5	<0.001	124.5	<0.001	99.9	<0.001	75.8	<0.001
k16	non-breeding adult female	11	26.02.03	10.04.15	None.	94.5	<0.001	152.6	<0.001	170.6	<0.001	3.2	0.060	3.6	0.059
t46	juvenile female	6	11.04.10	07.07.15	none.	91.1	<0.001	150.7	<0.001	175.5	<0.001	18.2	<0.001	-	-
k39	adult male	12	04.04.03	10.04.15	N/A	-	-	179.1	<0.001	178.2	<0.001	140.6	<0.001	141.1	<0.001

290

291 **Table 2.**

Measure	Category	Description	*F* value	*P* value	PC1 correlation value (-1 – 1)	PC2 correlation value (-1 – 1)
1. Absolute average height of surface	Height	Average greyscale value	10.7	<0.001	0.82	-0.29
2. Relative average height of surface	Height	Average difference between greyscale values above average	15.6	<0.001	0.84	-0.28
3. Root mean square height of surface	Height	Root mean square (RMS) greyscale value	9.6	<0.001	0.64	0.60
4. Maximum peak height of surface	Height	Value of maximum greyscale peak above average	49.4	<0.001	0.65	0.23
5. Average maximum peak height	Height	Average value of 10 highest greyscale peaks above average	53.5	<0.001	0.72	0.30
6. Minimum valley depth	Height	Value of lowest greyscale trough found below the average greyscale value	12.9	<0.001	0.54	0.46
7. Average minimum valley depth	Height	Average value of 10 lowest greyscale troughs found below the average greyscale value	51.6	<0.001	-0.64	0.56
8. Average height	Height	Average height of greyscale peaks	0.3	0.57		
9. Ten-point average height	Height	10-point moving average value of 10 greyscale peaks	0.3	0.57		
10. Maximum skew	Hybrid	Degree of symmetry of the surface heights about the mean plane	10.8	0.002	-0.78	0.62
11. Summit density	Hybrid	Number of greyscale peaks per unit area	149.7	<0.001	0.16	0.73
12. Maximum kurtosis	Hybrid	Prominence of inordinately high peaks and/or deep valleys	2.3	0.121		
13. Root mean square gradient of surface	Hybrid	Root mean square (RMS) of greyscale slopes, evaluated over all directions	9.6	0.002	0.47	0.26
14. Developed interfacial area ratio	Hybrid	Percentage of additional surface area contributed by the texture as compared to an ideal plane the size of the measurement's region	20.9	<0.001	0.90	-0.09
15. Core roughness depth	Functional	Proportion of dataset occupied by the core	7.854	0.006	0.33	0.58
16. Average peak height above core	Functional	Average difference in greyscale between peaks above the maximum core greyscale value versus the maximum core greyscale value	14.89	<0.001	0.93	-0.09

17. Average valley depth below core	Functional	average difference in greyscale between toughs below the minimum core greyscale value, and the minimum core greyscale value	7.842	0.009	0.39	-0.42
18. Surface bearing area ratio	Functional	Proportion of the surface that consists of peaks above the core greyscale value	12.3	<0.001	-0.30	-0.47
19. Autocorrelation length	Spatial	Horizontal distance of the autocorrelation function (ACF) that has the fastest decay to the value 0.2. Large value: surface dominated by low frequencies; low value: surface dominated by high frequencies	34.6	<0.001	0.18	0.02
20. Texture aspect ratio	Spatial	Ratio between the distance with the fastest to the distance with the slowest decay of the autocorrelation function (ACF)	9.8	0.002	0.82	-0.06

292

Supplement for "Synchrotron radiation-based X-ray tomography reveals sexual dimorphism in cementum incrementation"

1. *Macaca mulatta* sample preparation

This study is focused on the analysis of the right lower first molars (m1) from a sample comprised of nine sexually active females, three sexually inactive females, one sexually mature male and one juvenile female Rhesus macaque(s) (*Macaca mulatta*), raised under laboratory conditions and bred for biomedical research at the Primate Breeding Facility of Public Health England, Salisbury (UK) (Table 1). The unit was managed by the Defence Science and Technology Laboratory (DSTL) prior to 1st October 2009. The *Macaca mulatta* colony has been closed and self-contained since 1982, from animals originally imported from India between 1978 and 1982. All animals used here were routinely monitored and checked for primate-borne diseases of risk to humans (included hepatitis B, herpes B, and tuberculosis), and were humanely killed using an overdose of pentobarbital, under Home Office establishment licence 70-1707, due to being unfit for breeding or whole-animal scientific procedural use. No animal was killed for the specific purpose of this experiment. Once the animals were killed, their lower jaws were mechanically dislocated and removed by Public Health England. Lower jaws were then freeze-stored at -20 °C prior to further tissue preparation. To prepare first molar specimens for this study, lower jaws were first mechanically cleaned of soft tissue using surgical tools (scalpel, scissors and tweezers). The coronoid and angular processes were then removed using a handsaw. Once prepared, specimens were then bathed in tap water in a sealed plastic container, which was stored in a fume cupboard for three weeks (21 days). This procedure was adopted to rot away the periodontal ligament and alveolar soft tissue that could not be mechanically removed, in a

controlled manner. After three weeks, teeth were sufficiently loose within the jaw to be easily removed using surgical pliers, following further cleaning and removal of necrotic soft tissue. Although the majority of teeth were removed without damage, the anterior root of the left m1 was damaged in one specimen (l10). All teeth were removed for all animals, labelled and freeze-stored at -20 °C. The left and right m1 teeth of all animals were fixed in 10% paraformaldehyde (PFA) solution for 10 days to minimise risk of infection. Finally, the crowns of all teeth were removed using a Buehler IsoMet® Low Speed precision sectioning saw, equipped with an Acuthin™ blade (Buehler Ltd, Lake Bluff, IL, U.S.). Using the same saw and blade, the anterior and posterior roots of each m1 tooth were mechanically separated and the anterior root cut in half along its longitudinal axis. This was in order to minimise the proportion of dense dentine to cementum, to ensure that propagation-based phase contrast imaging (PPCI) through Synchrotron radiation-based computed tomography (SR CT) as employed here provides high image quality data, which can be detrimentally affected if the signal-to-noise ratio (SNR) is low due to tissues or materials with relative high X-ray absorption, such as dentine. Processed tooth roots were then placed on top of 'Ripmax' 2 mm-thick carbon fibre rods (CR200600; Ripmax Ltd, Enfield, UK) cut into 1.5 cm lengths, using Loctite® super glue (Liquid ethyl cyanoacrylate super glue, Loctite® brand; Henkel Corporation, Westlake, OH, U.S.). Carbon fibre rods are very rigid, yield a low X-ray absorption and do not create any significant X-ray scatter, as opposed to metallic sample holders.

2. Cementum texture analysis

The 16-bit greyscale nature of PPCI-CT volumes offers a rich source of comparative data in terms of greyscale 'texture'. Texture is here defined as the spatial organisation of greyscale

distribution within cementum PPCI-CT data. By studying greyscale values as a 'third dimension', several measures commonly used in surface profiling studies can be applied to PPCI-CT cementum data. 3D surface profiling is a commonly used technique in both tribology and biology, with measures established for tribology being increasingly applied to studies of dental micro-wear (18). These comprise height measures (the distribution of greyscale values above and below the average value for the surface), spatial measures (the direction and spatial periodicity of greyscale values across the *x*- and *y*-axis), hybrid measures (combining information present in both the *x*- and *y*-axis with the '*z*-axis' provided by greyscale values) and 'functional' measures that characterise volumetric information based on the material ratio of the surface in question (the ratio between the intersecting area of a hypothetical plane passing through the surface at a given height, and the cross-sectional area of the surface, typically between 10% and 80% of the maximum surface height known as the 'core'; 18). 20 measures were used here and are described in Table 2. Measures were applied in an automated fashion using a custom function in Matlab (R2016a; The MathWorks, Inc., Natick, MA, U.S.) (DOI: Appendix 1).

The applicability of the automated texture characterisation measures adopted here, and their discriminatory power for characterising greyscale value distributions, were tested on a sample of model images of controlled greyscale value distributions. A series of images was created of incremental greyscale value surfaces, designed with differing degrees of increment contrast and a range of increment counts (Fig. S1) (based on uni-directional Gaussian distributions – see DOI: Appendix 2 for Matlab script). Measures were then retrieved for each image, and their results were compared, using both ANOVA comparisons and Principal Component Analysis (PCA) (Table S1). Results were also compared to the results of measures derived from five images composed of randomly generated greyscale

values between 0 and 255, in order to attest whether measurements were intuitive to 'real' differences in 3D textures and resistant to noise.

The performance of each measure was assessed by comparison between the calculated values and the values predicted for each surface model, based on their image contrast and increment count. It was predicted that (a) models of increasing increment contrast will provide larger values for relative height measures (e.g. maximum peak height of surface, minimum valley depth), as there will be increasing differences between the average greyscale values of light (high greyscale values) versus dark (low greyscale values) increments, (b) models of increasing increment count will provide larger greyscale values for relative height measures, as there will be a higher proportion of pixels occupying the highest/lowest greyscale values, (c) increment count will have a more pronounced effect on functional measures relative to increment contrast, as higher counts within the same area will create thinner increments and so more fundamentally change the material ratio of the respective surface, (d) increment count will have the greatest control on hybrid and spatial measures, as higher increment counts will have a greater effect on the directionality of a surface and (e) increment models will all result in substantially different values for all measures compared to random greyscale value models.

Both ANOVA and PCA comparisons between calculated and predicted values for each measure suggested that the measures adopted here faithfully interpret discrete aspects of surface texture. All ANOVA comparisons between incremental models led to significant results (Table S1). Calculated results were also broadly comparable with those predicted for each model. Values of all height measures were considerably higher in high-increment count models, and high-contrast models had significantly higher values than low-contrast models of equal increment count, apart from average height. Although hybrid measurements produce

significant differences between samples, their correlation with increment patterns are less intuitive. All hybrid parameters, apart from developed interfacial area ratio, show strong positive correlation with increment count. But only developed interfacial area ratio shows significant (negative) correlation with increment contrast. All functional measurements produced significant correlation with increment count, with only surface bearing area ratio being negative. However, only core roughness depth and surface bearing area ratio had a significant (positive) correlation with increment contrast. Both spatial parameters had significant positive correlation with increment count and increment contrast. Finally, the most significant differences in all comparisons were between increment models and random greyscale value models.

PCA of greyscale value models reflected the results of ANOVA comparisons. Figure S2 highlights a significant separation along principal component 1 (84.8% of total variance) between all increment models and random greyscale value models. Models of varying increment contrast and count were significantly separated along principal component 2 (9% of total variance) in a predictable manner, with a negative, linear correlation between the component 2 value and increment count and contrast. These results suggest that the majority of measures adopted here provide meaningful values that discern ‘real’ patterns in greyscale values, and can thus be applied to cementum data. When applied to our cementum data, the automated texture algorithm was confined to the central 100/500 pixels of each PPCI-CT slice, avoiding any cracks found within the slice.

Figure S1.

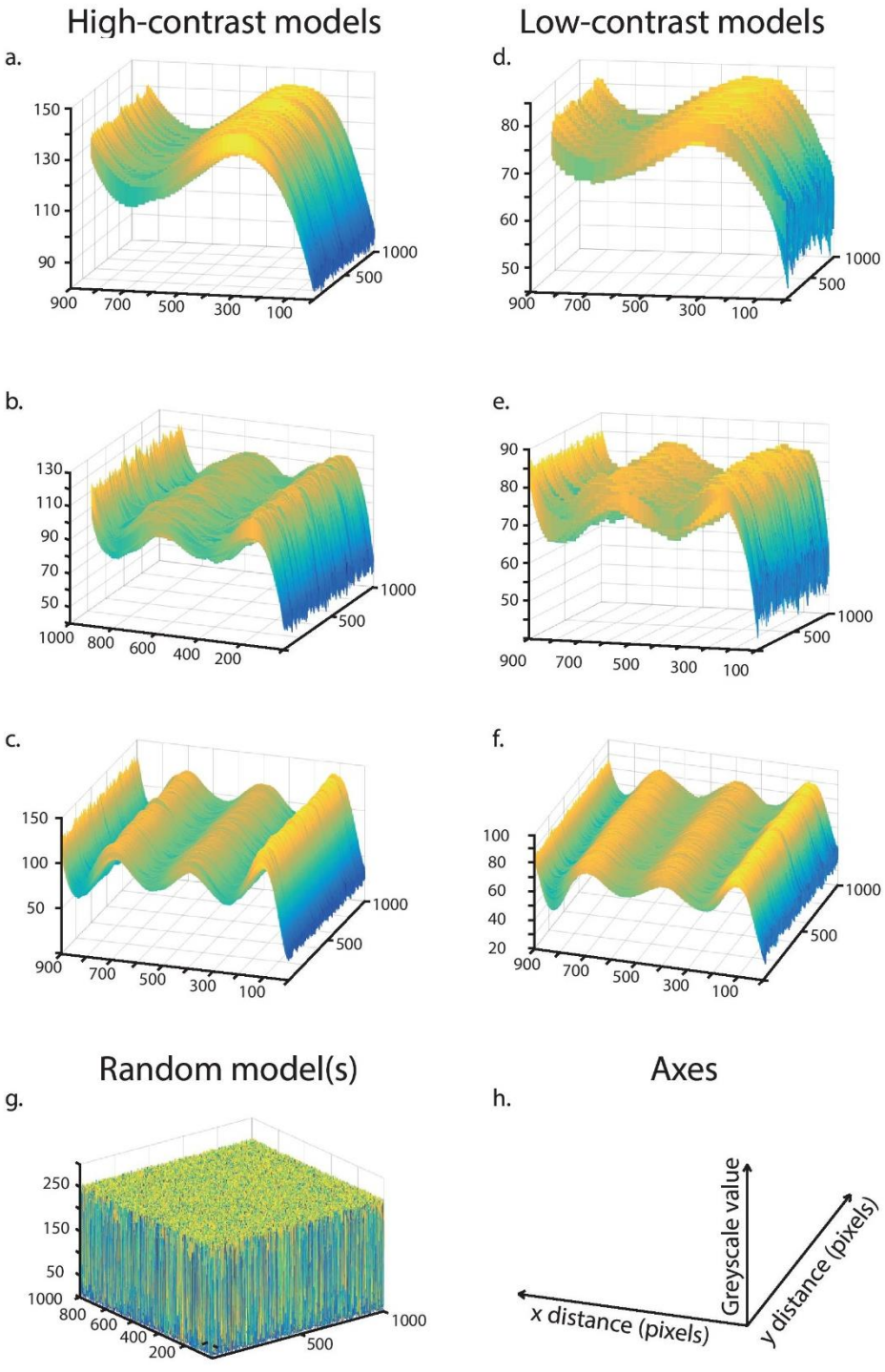
High-contrast models
Low-contrast models
a.
d.
b.
e.
c.
f.
Random model(s)
Axes
g.
h.
Greyscale value
x distance (pixels)
y distance (pixels)

Figure S1. Incremental models used to test the sensitivity of automated texture measures. **a-c**, High contrast models of increasing increment count. **d-f**, Low contrast models of increasing increment count. **g**, Random model of greyscale noise.

Figure S2.

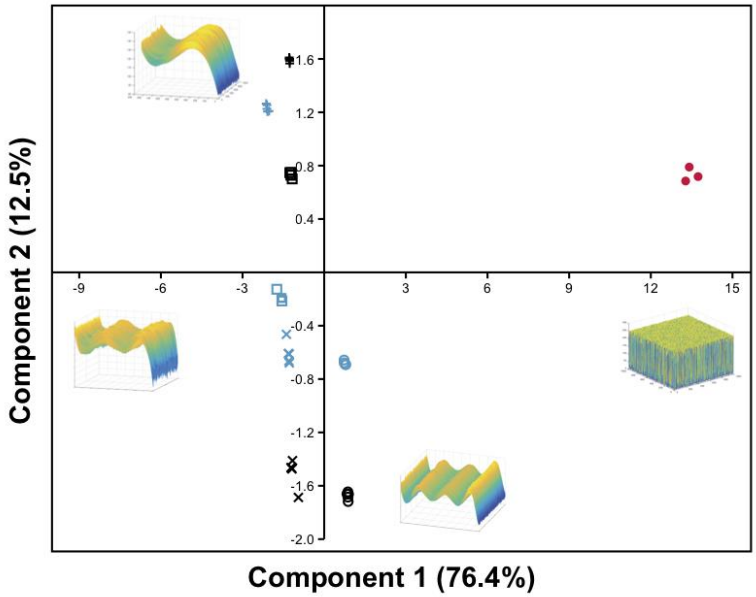

Key:

+	Low contrast; 1 increment
□	Low contrast; 2 increments
×	Low contrast; 3 increments
○	Low contrast; 4 increments
+	High contrast; 1 increment
□	High contrast; 2 increments
×	High contrast; 3 increments
○	High contrast; 4 increments
●	Random greyscale distribution

Figure S2. Results of PCA analysis of increment models. Component 1 represents surface roughness (texture spacing, amplitude and directionality). Component 2 represents increment contrast (distance of peaks/valleys from core, proportion of surface comprised by core).

Table S1.

Measure	*F*	*p*	Correlation with increment count			Correlation with increment contrast		
			r^2	*p*	Positive/negative	r^2	*p*	Positive/negative
Absolute average height of surface	>100	<0.001	0.5	<0.001	positive	0.98	<0.001	positive
Relative average height of surface	>100	<0.001	0.5	<0.001	positive	0.98	<0.001	positive
Root mean square height of surface	>100	<0.001	0.54	<0.001	positive	0.99	<0.001	positive
Average peak height	>100	<0.001	0.67	<0.001	positive	0.44	0.001	positive
Maximum peak height	>100	<0.001	0.63	<0.001	positive	0.52	<0.001	positive
Minimum valley depth	>100	<0.001	0.95	<0.001	positive	0.3	0.01	positive
Average minimum valley depth	>100	<0.001	0.93	<0.001	positive	0.32	0.01	positive
Average height	>100	<0.001	0.96	<0.001	positive	0.4	0.06	positive
Ten-point average height	>100	<0.001	0.89	<0.001	positive	0.51	0.001	positive
Maximum skew	>100	<0.001	0.96	<0.001	positive	0.15	0.08	negative
Summit density	>100	<0.001	0.99	<0.001	positive	0.03	0.47	negative
Maximum kurtosis	>100	<0.001	0.95	<0.001	positive	0.02	0.52	-
Root mean squared gradient of surface	>100	<0.001	0.99	<0.001	positive	0.02	0.5	-
Develop interfacial area ratio	>100	<0.001	0.02	0.46	-	0.29	0.02	negative
Core roughness depth	>100	<0.001	0.23	0.003	positive	0.4	0.003	positive
Average peak height above core	>100	<0.001	0.42	0.008	positive	0.007	0.73	-
Average valley depth below core	>100	<0.001	0.99	<0.001	positive	0.03	0.49	positive
Surface bearing area ratio	>100	<0.001	0.74	<0.001	negative	0.37	0.005	positive
Autocorrelation length	>100	<0.001	0.96	<0.001	positive	0.96	<0.001	positive
Texture aspect ratio	>100	<0.001	0.98	<0.001	positive	0.98	<0.001	positive

Table S1. Results of ANOVA comparisons between increment models for each texture measure, and least-squares regression between values for individual measures and increment count and contrast, respectively.

3. Cementum increment tortuosity analysis

A principal record of cementum growth is the structure and shape of its constituent increments (9). Several discrete life history variables have previously been traced in the relative shape and thickness of cementum increments in mammal taxa (2). We here used image processing to 'straighten' PPCI-CT cementum data, and to then isolate individual cementum increments in straightened data and analyse their geometric two-dimensional (2D) tortuosity. Tortuosity can be defined by the ratio between the actual length followed by a path, versus the geometric distance between its endpoints (Fig. 1f-i). Within these straightened datasets, the cemento-dentine boundary provides a straight line upon which transects of increments vary, so that measured tortuosity can be compared between datasets relative to this layer found in each dataset. As the boundary will be the site of initial growth of cementum, we believe this provides an accurate means of estimating the tortuosity of increments relative to each other.

The 30 randomly selected PPCI-CT slices for each *Macaca mulatta* individual were subjected to a novel algorithm implemented in Matlab (DOI: Appendix 3), where increments were individually isolated in a stepwise fashion from the outermost increment. Isolation of increments was attempted along radial transects across the *x*-axis of each slice (Fig. S3a). For every pixel along the *x*-axis, *y*-axis vectors were produced (Fig. S3). In straightened PPCI-CT data, 'light' increments will produce peaks in greyscale values above average (Fig. S3). Hence, the first and last pixel of each light increment can be easily identified using the second order derivative of Greyscale values along each *y*-axis vector (Fig. S3b). These calculated derivative values were recorded for each vector, along with their distance in pixels, in a new dataset providing information on the location, shape and thickness of each individual increment within the CT slice. For each increment, this dataset was then used to

compute an increment model consisting of a binary image of a10-pixel thick virtual increment, following the measured trajectory of the respective increment (Fig S3c).

Once increments had been isolated (Fig. S3b) and modelled (Fig. S3c), the path lengths of their models were measured in Matlab by calculating the *y*-axis difference between every pixel along the *x*-axis trajectory of the model using the 'diff' function (Fig. S3d). Differences were then multiplied by -1 (to make sure that all values were positive) and summed up. The sum of the differences was then added to the *x*-axis length of the model. Shortest possible path lengths were calculated between the two endpoints of the increments as the hypotenuse between their *x*-axis and *y*-axis coordinates (Fig. 1h-i). Finally, tortuosity was calculated as the ratio between the calculated path length and shortest path length (DOI: Appendix 4).

Before experimental cementum data was analysed using this algorithm, its accuracy for isolating increments, and precision with increments isolated using human vision, were validated. First, a series of 10 binary (black and white) digital 2D images was created in ImageJ/Fiji (Version 2.0) (15). These consisted of one-pixel thick white lines, drawn across a black background in increasingly complex wave patterns using the 'Freehand' tool (Fig. S4). The lengths of these lines were calculated algebraically using the 'Measure' tool and the minimum length between their end points were measured using the 'Analyze skeleton' tool to calculate their Euclidian distance. Tortuosity was calculated for each image as the ratio between these values. These images were then subjected to our tortuosity calculation algorithm. The accuracy of our algorithm could thus be assessed as the difference between the tortuosity calculated in ImageJ/Fiji and the tortuosity calculated by our algorithm for each phantom.

To test the precision of our algorithm with increment isolation using human vision, the outer three increments of three PPCI-CT slices, to which the algorithm had been applied for tortuosity analysis, were isolated by hand in Avizo image analysis software (version 9.3; Thermo Fisher Scientific), using a Wacom Cintiq 22HD Creative pen display. In the "Edit new Label Field" toolkit of Avizo, each increment was hand-traced using the Wacom interactive pen and assigned its own label. Each label was then saved as its own binary Tiff file. For each increment, the *y*-axis position for each pixel along the *x*-axis was then compared between increment models created using our algorithm and human vision. A difference of 20 pixels was arbitrarily assigned as the threshold for defining precise (< 20-pixel difference) versus non-precise (> 20-pixel difference) comparisons, as this represents a full departure of a 10 pixel-thick increment.

Tortuosity estimates of digital phantoms of known properties were within 0.05 of known values for each phantom (Table S2). We interpret this as suggestive that our tortuosity estimates are accurate, as this is an order of magnitude less than the average difference in ranked tortuosity values acquired during our primary experiment (n = 1950, mean ranked tortuosity difference = 0.016). Comparison between algorithmically isolated increments and manually isolated increments also suggested that our algorithm offers a precise method for isolating cementum increments in PPCI-CT data. For each dataset, apart from the third increment of slice three, mean distances between algorithmically and manually isolated increments were less than four pixels (2.65 μm), with a maximum difference of 12 pixels (7.92 μm) (Fig. S5). This is well below the 20-pixel threshold assigned for these comparisons.

Figure S3.

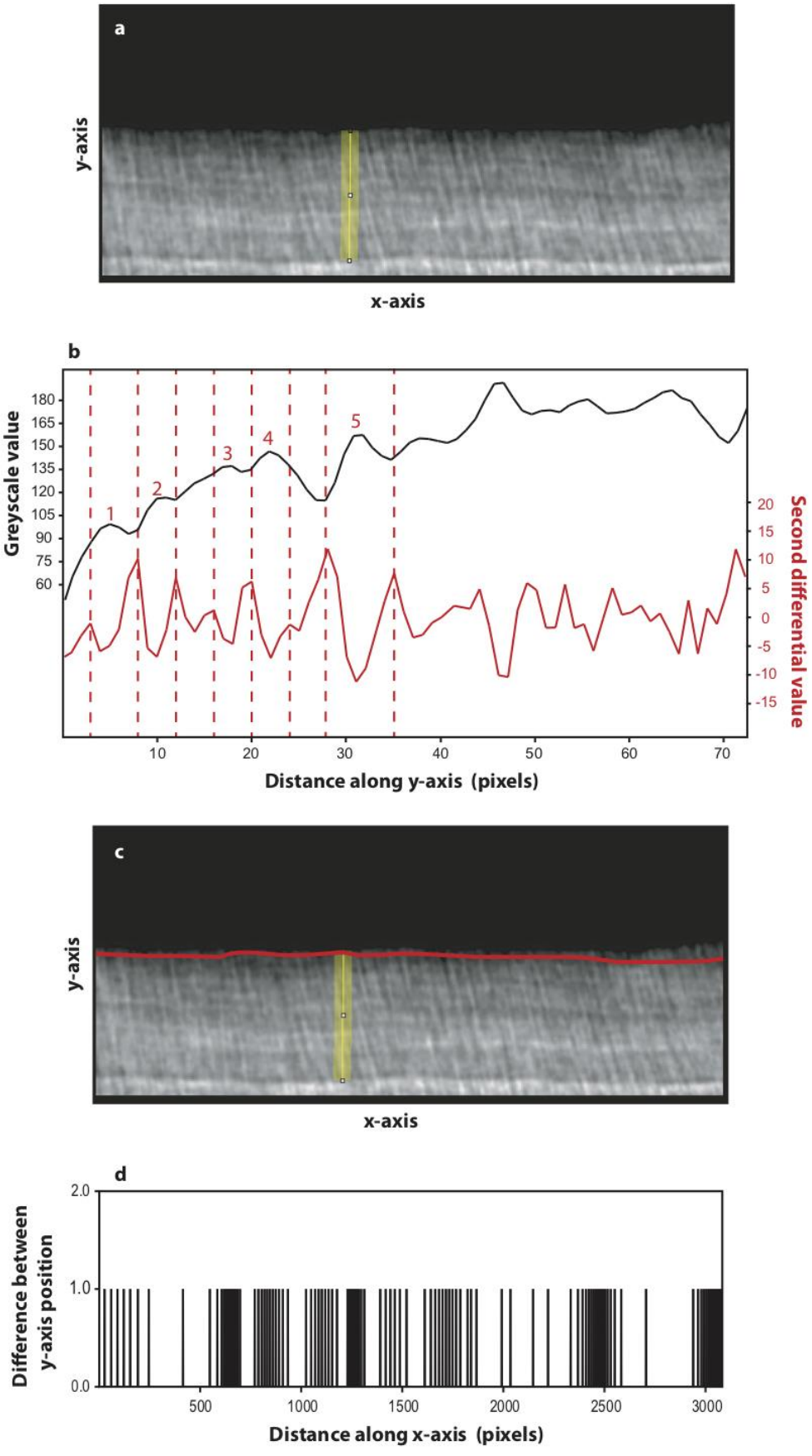
a
y-axis
x-axis
b
Greyscale value
180
165
150
135
120
105
90
75
60
1
2
3
4
5
Second differential value
20
15
10
5
0
-5
-10
-15
10
20
30
40
50
60
70
Distance along y-axis (pixels)
c
y-axis
x-axis
d
Difference between y-axis position
2.0
1.0
0.0
500
1000
1500
2000
2500
3000
Distance along x-axis (pixels)

Figure S3. Cementum increment isolation and tortuosity analysis. a, Straightened image of the cementum of male individual k39 with *y*-axis transect plotted along yellow line. **b**, Plot of greyscale values along transect in **a** (black line) and results of calculation of the second order derivative of per-pixel y-axis position between pixels (red line). Peaks in the red line correspond to the beginning and end of each light increment (represented by peaks in greyscale values along the black line), denoted using dashed red lines for the first five increments. **c**, Modelled outermost increment based on isolation using y-axis second order derivative peak locations, following the red line. **d**, Plot of per-pixel difference in position along the *y*-axis for every pixel along the *x*-axis of the increment model shown in **c.**

Figure S4.

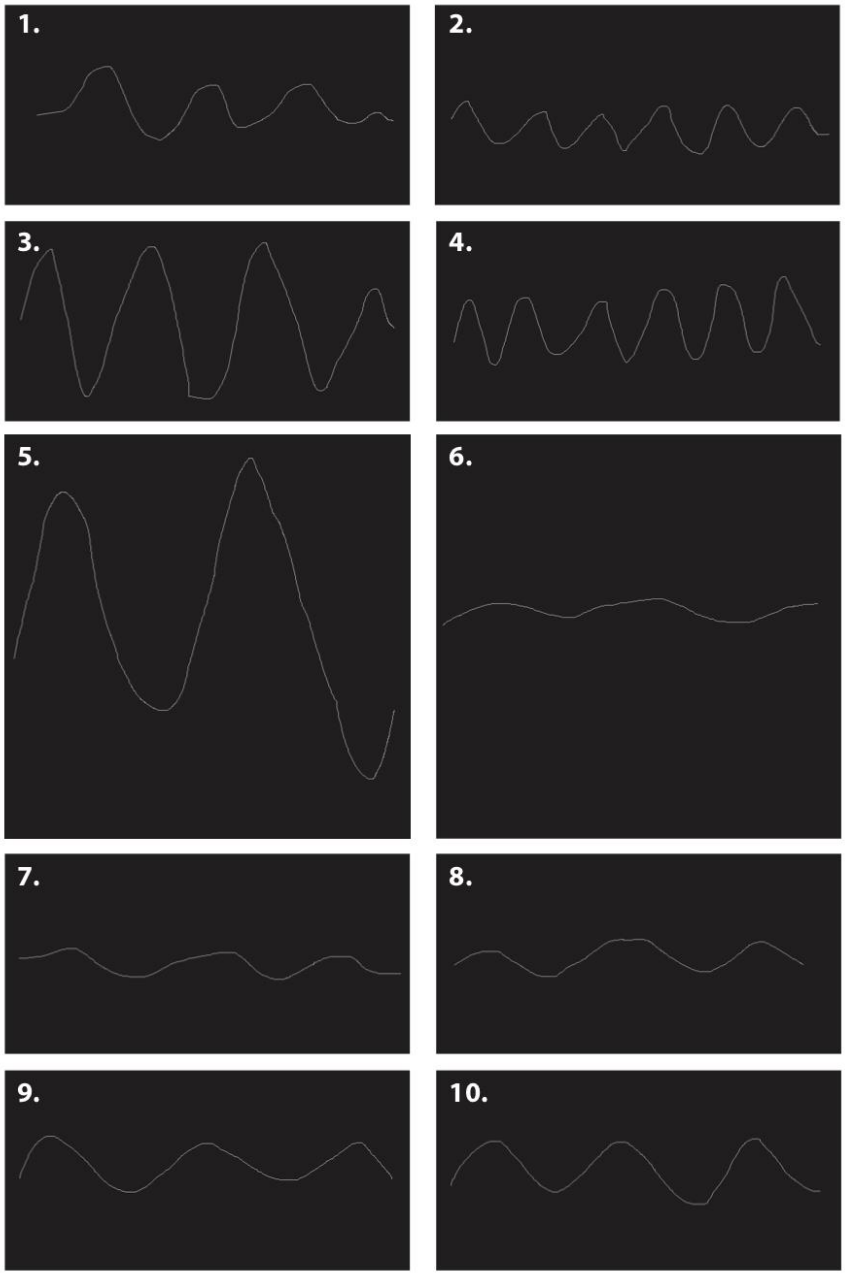

Figure S4. Digital phantoms of known length designed to test the accuracy of the cementum increment tortuosity algorithm. The number of each image corresponds to the numbers used in **Table S2**.

Figure S5.

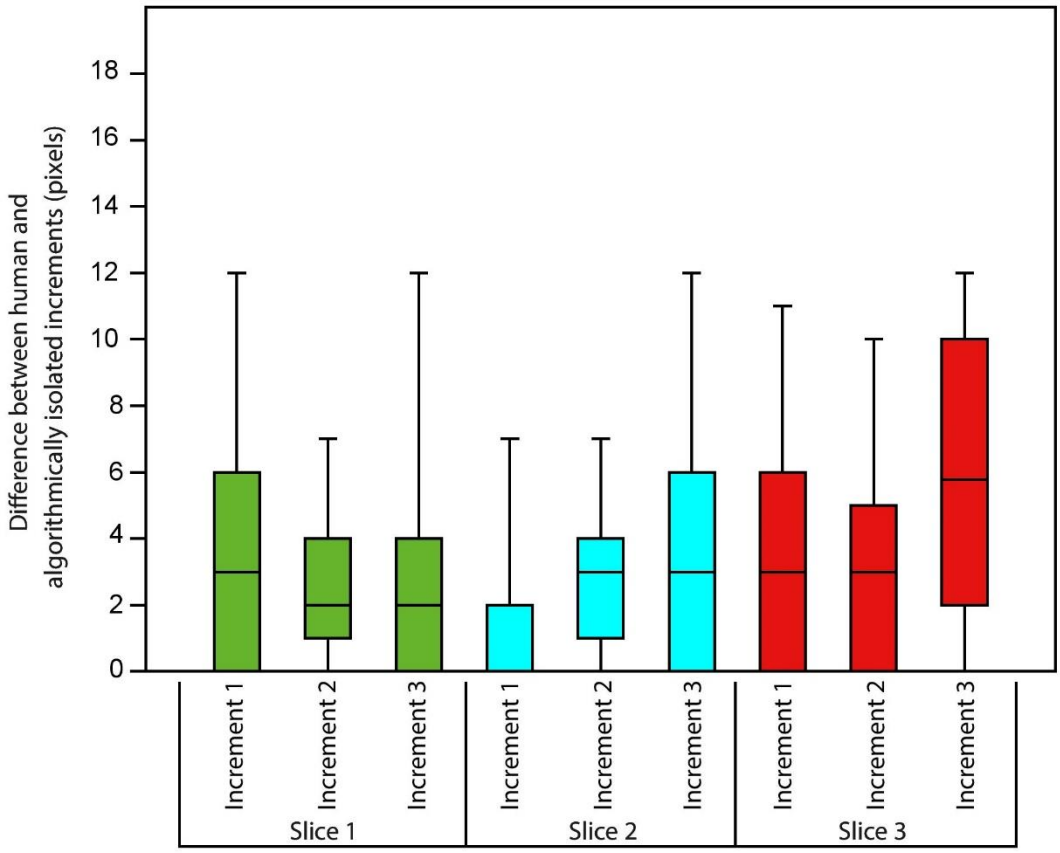

Figure S5. Comparison between manually isolated and algorithmically isolated cementum increments. Boxes represent the inter-quartile ranges around the mean difference (black line) in pixels between algorithmically isolated and manually isolated versions of the same increment in 2D space. Whiskers represent the highest differences between human and algorithmically isolated attempts for each increment.

Image	Length (pixels)	Euclidian distance (pixels)	Algebraically calculated tortuosity (1)	Algorithmically calculated tortuosity (1)	Difference between tortuosity values (1)
1	1355.675	882.110	1.53	1.52	0.01
2	1633.565	932.695	1.75	1.7	0.05
3	2834.685	930.000	3.05	3.02	0.03
4	2383.204	906.020	2.63	2.66	0.03
5	2982.082	948.675	3.14	3.07	0.07
6	1025.169	927.573	1.11	1.11	0.00
7	1083.921	944.765	1.15	1.15	0.00
8	1031.000	862.000	1.20	1.19	0.01
9	1235.000	920.000	1.34	1.32	0.02
10	1345.000	912.000	1.48	1.44	0.03

Table S2. Comparisons between algebraically calculated and algorithmically calculated tortuosity values for digital phantoms of known length.